Two-electron selective coupling in an edge-state based conditional phase shifter

Laura Bellentani,[1] Gaia Forghieri,[2] Paolo Bordone,[1,2] and Andrea Bertoni[1]
[1]*S3, Istituto Nanoscienze-CNR, Via Campi 213/A, 41125 Modena, Italy*
[2]*Dipartimento di Scienze Fisiche, Informatiche e Matematiche, Università degli Studi di Modena e Reggio Emilia, Via Campi 213/A, 41125 Modena, Italy*

(Received 16 March 2020; revised 25 June 2020; accepted 25 June 2020; published 13 July 2020)

We investigate the effect of long-range Coulomb interaction on the two-electron scattering in the integer quantum Hall regime at bulk filling factor two. We compute the dynamics of the exact two-particle wave function by means of a parallel version of the split-step Fourier method in a 2D potential background reproducing the effect of depleting gates in a realistic heterostructure, with the charge carrier represented by a localized wave packet of edge states. We compare the spatial shift induced by Coulomb repulsion in the final two-electron wave function for two indistinguishable electrons initialized in different configurations according to their Landau index and analyze their bunching probability and the effect of screening. We finally prove the feasibility of this device as a two-qubit conditional phase shifter able to generate controlled entanglement from product states.

DOI: 10.1103/PhysRevB.102.035417

I. INTRODUCTION

Over the years, single-electron and two-electron interference have been realized in a large variety of devices operating in the integer quantum Hall regime, making them an ideal platform for electron quantum optics [1–5] and a possible candidate for quantum computing architectures based on flying qubits [6–9]. Early implementations of the electronic Mach-Zehnder interferometer (MZI) at bulk filling factor one proved self-interference of the electron wave function and the viability of coherent transport in edge states [10–12] but are affected by a fundamental geometrical limit that jeopardizes their concatenation in series. A new geometry has been then proposed recently by Giovannetti *et al.* [13], where the scattering between the first two copropagating edge channels is generated by an alternative design of the beam splitter [14,15]. The scalability of this new approach allows, in principle, the implementation of two-qubit logic gates, as the Hanbury-Brown-Twiss interferometer [16–21], where exchange symmetry induces the Hong-Ou-Mandel (HOM) effect [22–26] and the conditional phase shifter (CPS) for entanglement generation [27]. Together with the effect of electron-electron interaction, the interplay between the geometry of the device and the electron correlations plays a crucial role in the quantum logic gate operation [28].

In the literature, the numerical simulation of Hall interferometers usually exploits the chirality of edge states to model electron transport in effective 1D schemes [8,29]. Moreover, delocalized edge states are often considered as current-carrying states. Differently, we simulate single and two-electron transport in a full-scale 2D Hall nanodevice by using a time-dependent framework based on the split-step Fourier method [31], where electrons are described by single-charge wave packets. We numerically setup the 2D potential landscape generated by modulation gates in order to compute the edge states with the exact shape induced by our design of the confining barrier; such states are then linearly combined with a Gaussian weight function. With a large but affordable computational cost [28], this method provides access to the dynamical properties of an interacting system of electrons directly from the exact two-particle state and allows us to introduce in a rigorous way electron-electron repulsion. This proved to be relevant in devices whose functioning is based on two-electron scattering, as the HOM interferometer in Ref. [22], where we observe the transition from an exchange-driven to a Coulomb-driven bunching of strongly-localized wave packets. Moreover, by encoding the initial electron state in a Gaussian wave packet [12,15,22], we reproduce the injection of a *hot electron* by means of single-electron sources [32–38], as recently proposed theoretically by Riu *et al.* with quantum dot pumps [39].

In this paper, our full-scale numerical approach is applied to simulate two-electron scattering in the active region of a solid-state conditional phase shifter [28], as the one depicted in Fig. 1(a). The figure shows the interferometer pattern created by the external potential (gray structure) induced by modulation gates and the electron wave packets at an intermediate time [30]. The design of the two multichannel MZIs in the integer quantum Hall (IQH) regime is devised in Ref. [13] and simulated in Ref. [15]; in our proposal for a conditional phase shifter, two of these interferometers are concatenated in parallel, as schematically represented in Fig. 1(b), and generate four channels, two of them (ground and first excited) running at each side of the 2DEG. Self-interference in each MZI is affected by a selective Coulomb interaction that couples only those electron states localized in the first excited channels. The distance between the two electron paths is decreased by a potential mesa, where the bulk filling factor is one, so that their mutual interaction is increased. Figure 1(c) shows the band structure of the active region for Coulomb coupling (yellow box). Here, the spatial confinement of the transverse probability distribution for the single-electron wave function (dashed black line) ensures the absence of tunneling between counterpropagating channels.

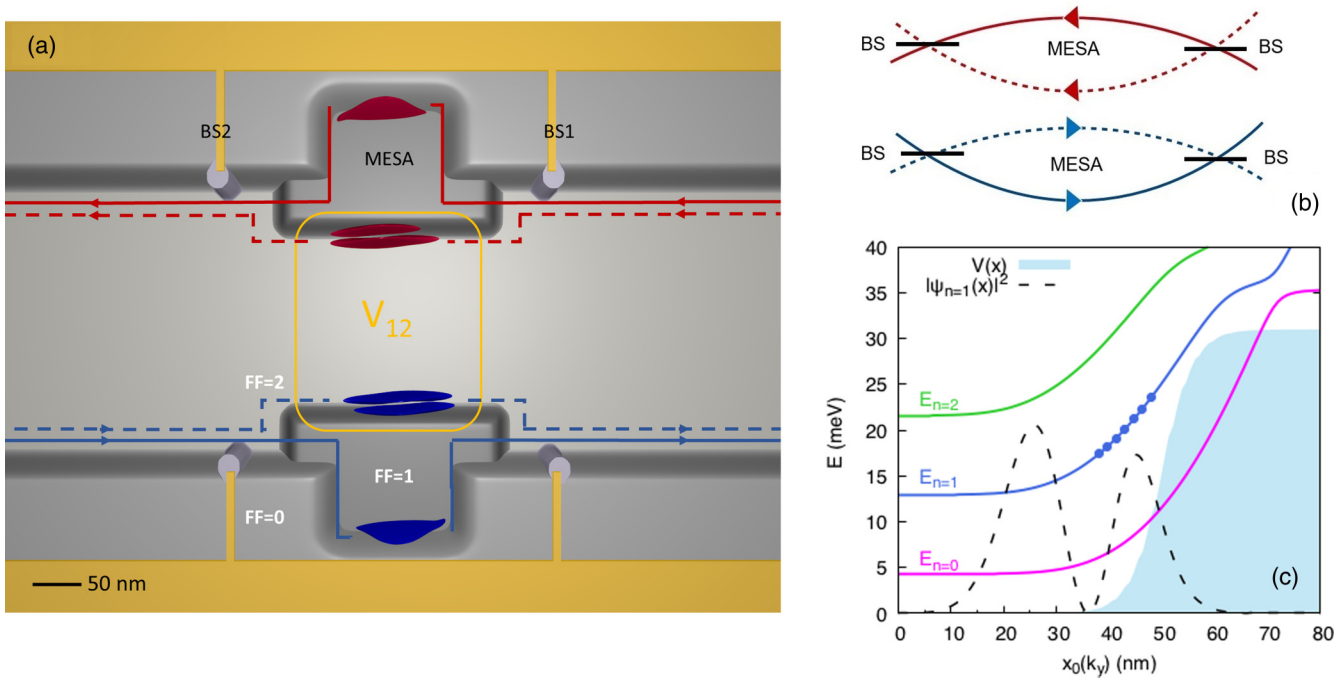

FIG. 1. (a) Two parallel multichannel MZIs, with the design proposed in Ref. [15], define a conditional phase shifter **T** in the IQH regime. Two edge channels copropagate at each side of the device due to the bulk filling factor two. The Landau level with index $n = 1$ (dashed line) is localized at one edge of the step potential that lowers the filling factor to one (labeled with MESA) between the two beam splitters (BS1, BS2). The edge channel with $n = 0$ (solid line) is confined at the other edge of the mesa. Thanks to the spatial separation between the paths with $n = 0$ and $n = 1$ in this region, an electron accumulates different phases in the two channels. The yellow squared box identifies the active region where electrons interact; the two-electron Coulomb repulsion V_{12} can be increased or decreased by tuning the width of the MESA. The red and the blue wave packets show the single-electron density probability of the counterpropagating charges, computed at an intermediate time of their evolution with our numerical approach. See also the Supplemental Material of Ref. [30] for an animation of the two-particle dynamics. (b) Schematic representation of the device. Two single-electron Mach-Zehnder interferometers are concatenated in parallel to realize a conditional phase shifter. (c) Band structure of the active region of the conditional phase shifter of panel (a) at one of the two edges of the device. The first three Landau levels ($n = 0, 1, 2$) are displayed as solid lines labeled with E_n; the dots at $n = 1$ identify the edge states combined to generate a Gaussian wave packet in the second channel with $\sigma = 40$ nm and a central energy $E^0 = 21$ meV. The single-electron probability distribution of the electron wave packet in the transverse direction of the second edge channel is also displayed (dashed line).

According to its strength, Coulomb coupling affects the two-electron state at the output of the device, by selectively rotating only the component of the wave function with both electrons in the first excited states; this realizes the transformation [27,28]

$$\mathbf{T}(\gamma) = \begin{pmatrix} 1 & 0 & 0 & 0 \\ 0 & 1 & 0 & 0 \\ 0 & 0 & 1 & 0 \\ 0 & 0 & 0 & e^{i\gamma} \end{pmatrix}. \tag{1}$$

The present device provides the ideal playground for our numerical model: The geometrical parameters of the potential landscape, e.g., the length of the coupling region and the distance between the channels, affect significantly the strength of Coulomb repulsion and therefore the corresponding angle γ.

This paper is organized as follows. In Sec. II we summarize the numerical model of localized carriers in edge states in the IQH regime and our simulation approach of the two-electron device. Then, Sec. III A describes the selective action of the Coulomb interaction in a simple geometry for the active region, with two sharp potential barriers at the edges of the 2DEG. We analyze how the Landau level band structure affects the effectiveness of electron-electron repulsion and calculate the total amount of energy exchanged during the two-electron scattering in Sec. III B. After computing the bunching probability for short interchannel distances, we include screening effects on the two-particle dynamics in Sec. III C. Finally, we adopt a more realistic model of the confining potential with smoothed Fermi-like barriers, and in Sec. III D we predict the γ factor expected in a full-scale conditional phase shifter.

II. PHYSICAL SYSTEM AND NUMERICAL MODEL

In our numerical simulations, two interacting electrons with charge $q = -e$ and an effective mass m^* propagate in a confined 2DEG on the xy plane and are immersed in a perpendicular magnetic field $\mathbf{B} = B\hat{z}$. The effect of the magnetic field on the electron transport is described in the Landau gauge, which introduces the vector potential $\mathbf{A}_i = Bx_i\hat{y}$ in the single-particle Hamiltonian H_i, with $i = 1, 2$ indicating the first or second electron, respectively. In the presence of Coulomb interaction V_{12} and a confining potential V, the two-electron

Hamiltonian reads:

$$H = \frac{(p_1 - qA_1)^2}{2m^*} + \frac{(p_2 - qA_2)^2}{2m^*} + V_1 + V_2 + V_{12}$$
$$= \sum_{i=1,2}\left(\frac{p_{x_i}^2}{2m^*} + \frac{p_{y_i}^2}{2m^*} + \frac{eBx_i p_{y_i}}{2m^*} + \frac{e^2B^2x_i^2}{2m^*} + V(\mathbf{r}_i)\right)$$
$$+ V_{12}(\mathbf{r}_1, \mathbf{r}_2). \quad (2)$$

Here, magnetic components of the kinetic operators in the Landau gauge clearly couples the x coordinate in the real space and the k_y coordinate in the reciprocal space, for each particle.

At the initial time, when the two counterpropagating electrons are distant, the mutual interaction is negligible ($V_{12} \simeq 0$) and each single-particle Hamiltonian H_i in Eq. (2) is separable on the real-space domain. By adopting the *ansatz* $\phi_i = \varphi_{n_i,k_i}(x_i)e^{ik_i y_i}$, the noninteracting Hamiltonian can be expressed in the effective 1D form

$$H_i\phi_i = \left[-\frac{\hbar^2}{2m^*}\frac{\partial^2}{\partial x_i^2} + \frac{1}{2}m^*\omega_c^2\left(x_i - x_i^0\right)^2\right. \quad (3)$$
$$\left. + V(x_i, y_i)\right]\varphi_{n_i,k_i}(x_i)e^{ik_i y_i}, \quad (4)$$

where k_i is the wave vector in the y direction of the reciprocal space, $|\omega_c| = eB/m^*$ is the cyclotron frequency, n_i is the Landau index, and $x_i^0 = -eBk_i/\hbar$ is the center of an effective parabolic confinement in the x direction induced by the magnetic field.

In the presence of a translationally invariant potential in the x direction, $V(x, y) = V(x)$, by selecting a wave vector k and Landau index n, we identify the eigenstates $\varphi_{n,k}(x_i)$ that diagonalize the single-particle effective Hamiltonian in 1D:

$$H^{\text{eff}}(x) = -\frac{1}{2m^*}\frac{\partial^2}{\partial x^2} + \frac{1}{2}m^*\omega_c^2(x - x^0)^2 + V(x). \quad (5)$$

The Hamiltonian above determines the localization of the electron wave function in the transverse direction of the device (orthogonal to the propagation direction), due to the presence of the magnetic confining potential, $V_B(x) = \frac{1}{2}m^*\omega_c^2(x - x^0)^2$ which adds to the external one, $V(x)$.

Note that in the bulk of the confined 2DEG, where $V(x) \simeq 0$, the eigenfunction $\varphi_{n,k}$ coincides with the eigenstate of an harmonic oscillator with frequency ω_c. In the presence of a non-negligible confining potential, the eigenstates of the effective Hamiltonian H_i^{eff} must be computed numerically, and their shape depends on the smoothness of $V(x)$. The single-particle wave function $\phi(x, y) = \varphi_{n,k}(x)e^{iky}$ is indeed called *edge state*, and it is composed by a delocalized plane-wave term in the longitudinal direction, e^{iky}, and a confined wave function $\varphi_{n,k}(x)$ in the transverse one. The corresponding eigenenergy for a given value of the quantum numbers n and k is

$$E_n(k) = \hbar\omega_c\left(n + \tfrac{1}{2}\right) + \epsilon_n(k), \quad (6)$$

which depends on the wave vector k only if $\epsilon_n(k) \neq 0$, i.e., in proximity to the confining edge barrier.

A. Gaussian wave packets as charge carriers

To simulate a flying-qubit implementation of the conditional phase shifter, we encode the electrons in Gaussian wave packets of edge states belonging to the same Landau level n:

$$\psi_\alpha(x, y) = \int dk F\left(k, k_\alpha^0, \sigma_\alpha\right)\varphi_{n,k}(x)e^{iky}. \quad (7)$$

The weight function $F(k, k_\alpha^0, \sigma_\alpha) = C\exp(-\sigma_\alpha^2(k - k_\alpha^0)^2)$ linearly combines edge states with different wave vectors k and a given Landau index n. The index α labels the translationally invariant region where the single-electron wave packet is initialized. The smoothness of the confining edge barrier, $V_\alpha(x)$, together with the central wave vector k_α^0 and the real-space broadening σ_α of the wave packet, determine the group velocity v_g^α of the electron state. As proved in the numerical simulations of single and two-electron dynamics in Ref. [12], Ref. [15], and Ref. [22]; the Gaussian wave packets in Eq. (7) maintain all the properties of edge states, i.e., the chirality and immunity to backscattering. Moreover, the Gaussian shape of the single-electron state is preserved much more efficiently with respect to alternative frameworks, as in the presence of a Lorentzian or exponential distribution in the energies.

In the present geometry, we identify two translationally-invariant regions, V_α and V_β, where the single-electron wave packet is initialized. The two interacting electrons are assumed to be injected in counterpropagating channels, and therefore the confining potentials must be characterized by the same smoothness but opposite bending, as in the geometry of the HOM interferometer from Ref. [22]. In order to include the fermionic antisymmetry of the two-electron wave function, the orbital single-electron wave packets ψ_α and ψ_β generated in the two initialization regions of the device are combined in the antisymmetric form

$$\Psi(\mathbf{r_1}, \mathbf{r_2}) = \frac{\psi_\alpha(\mathbf{r_1})\psi_\beta(\mathbf{r_2}) - \psi_\beta(\mathbf{r_1})\psi_\alpha(\mathbf{r_2})}{\sqrt{2}}. \quad (8)$$

We stress that the above wave function depends on four real-space coordinates: The memory burden needed to allocate numerically the corresponding 4D array (about 1 Terabyte in our numerical simulations) can be afforded only by exploiting the resources of supercomputing facilities with memory-distributed architectures and parallel techniques for high-performance computing. In particular, we distribute the two-particle wave function on a Cartesian topology of MPI processes, which maps the domain of the second particle (x_2, y_2).

B. The split-step method for time evolution

In our dynamic approach, the two-electron wave function $\Psi(\mathbf{r_1}, \mathbf{r_2})$ at initial time $t = 0$ in Eq. (8) is evolved by iteratively applying the evolution operator

$$U(\delta t) = e^{-i\frac{H_{12}\cdot\delta t}{\hbar}}, \quad (9)$$

with the Hamiltonian H_{12} defined in Eq. (2). In particular, we adapt the split-step Fourier method and the Trotter-Suzuky factorization to the present case of two interacting charges, as detailed in the following.

In the presence of non-negligible electron-electron interaction, $H_{12}(x_1, y_1, x_2, y_2)$ can be rewritten as

$$H_{12} = V(\mathbf{r}_1) + V(\mathbf{r}_2) + V_{12}(\mathbf{r}_1, \mathbf{r}_2) + T_x(x_1, x_2) + T_y(y_1, y_2), \tag{10}$$

with V single-particle external potential and

$$T_x = \frac{p_{x_1}^2}{2m^*} + \frac{p_{x_2}^2}{2m^*}, \tag{11}$$

$$T_y = \frac{p_{y_1}^2}{2m^*} + \frac{2eBx_1p_{y_1}}{2m^*} + \frac{e^2B^2x_1^2}{2m^*} + \frac{p_{y_2}^2}{2m^*} + \frac{2eBx_2p_{y_2}}{2m^*} + \frac{e^2B^2x_2^2}{2m^*}. \tag{12}$$

Equations (11) and (12) represent the 2D kinetic operators for two free electrons in a perpendicular magnetic field, projected on the x or y direction of the real space. The potential operator V is characterized by a diagonal representation in the real space, x_1y_1 and x_2y_2. The kinetic operator T_{x_1,x_2} is represented by a diagonal matrix in the 2D reciprocal space $k_{x_1}k_{x_2}$. The operator T_{y_1,y_2} is diagonal only in the 4D reciprocal space defined by $x_1k_{y_1}x_2k_{y_2}$. Finally, V_{12} couples the x and y coordinates, so that its diagonal representation is possible only in the 4D configuration space $x_1y_1x_2y_2$, which is the domain of the two-particle wave function.

According to the Trotter-Suzuky factorization method [31], the $U(t;0)$ operator for an evolution time $t = N \cdot \delta t$ is factorized into three exponentials:

$$\left[e^{-\frac{i}{\hbar}\delta t H_{12}}\right]^N = \left[e^{-\frac{i}{\hbar}\delta t\cdot(V_1+V_2+V_{12})}e^{-\frac{i}{\hbar}\delta t\cdot T_x}e^{-\frac{i}{\hbar}\delta t\cdot T_y}\right]^N, \tag{13}$$

so that Fourier transforms $\mathsf{F}_{x_1,x_2}(\mathsf{F}_{y_1,y_2})$ and antitransforms $\mathsf{F}^{-1}_{x_1,x_2}(\mathsf{F}^{-1}_{y_1,y_2})$ can be applied to switch from the real to the reciprocal space and to exploit the locality of the modified kinetic operators $T_x(x_1, x_2)$ $[T_y(y_1, y_2)]$ in the reciprocal space $[k_{x_1}, k_{x_2}]$ $([k_{y_1}, k_{y_2}])$. The evolution operator finally reads

$$U(t,0) = \left[e^{-\frac{i}{\hbar}\delta t\cdot(V_1+V_2+V_{12})}\mathsf{F}^{-1}_{y_1,y_2}e^{-\frac{i}{\hbar}\delta t\cdot T_{y_1,y_2}}\mathsf{F}_{y_1,y_2}\mathsf{F}^{-1}_{x_1,x_2}e^{-\frac{i}{\hbar}\delta t\cdot T_{x_1,x_2}}\mathsf{F}_{x_1,x_2}\right]^N. \tag{14}$$

C. Numerical modeling of the active region

We initially describe the active region of the device in Fig. 1(a) with a simplified geometry to expose the selectivity of Coulomb coupling for two electrons initialized in the first two Landau levels $n = 0, 1$. In this model, the two-electron wave function propagate in a confined 2DEG with two sharp barriers in the transverse direction of the device. Thus, the external potential in the single-particle Hamiltonian is $V(x) = V_b[\Theta(x_L - x) + \Theta(x - x_R)]$, where V_b is the height of the barrier, x_L and x_R identify the turning points at the edges, and $\Theta(x)$ is the Heaviside function.

Figure 2 compares the band structure of the first three Landau levels $E_0(x_0)$, $E_1(x_0)$, and $E_2(x_0)$ (solid lines) with the transverse shape of the external potential profile $V(x)$ at the right side of the initialization region. The dots on the two Landau levels identify the centers $x_0(k)$ of the eigenstates involved in the linear combination of Eq. (7) for two single-electron wave packets in the ground $(n = 0)$ or in the excited $(n = 1)$ channel. The present device operates at bulk filling factor two, i.e. the first two Landau levels are available at the energies involved in our operating regime, which are well below the third Landau level with a minimum energy $E_2 = 21$ meV. We observe that, for a central energy $E^0 \approx 15$ meV and a real-space broadening $\sigma = 40$ nm, the first Landau level is characterized by a sharper bending, thus resulting in a higher group velocity (or, equivalently, a smaller magnetic mass) for a Gaussian wave packet initialized in $n = 0$ with respect to the same in $n = 1$. We therefore expect that Coulomb repulsion determines a larger spatial shift δy for two electrons localized in $n_1 = n_2 = 1$ with respect to alternative configurations. This effect is further enhanced by the different probability distribution of the single-electron wave packets with $n = 0, 1$ in the transverse direction of the device, displayed in Fig. 2. The initial wave packet with $n = 1$ has a larger probability in the bulk of the 2DEG. Note, however, that both wave packets are mostly localized at positive values of the real-space domain in the x direction, thus ensuring a negligible overlap with the counterpropagating state, which is symmetric with respect to the origin. Then, for a distance $d > 100$ nm between the edges, the two-electron scattering is purely driven by Coulomb interaction, and no interchannel tunneling is present.

III. RESULTS

In the following, we discuss the selective coupling of two electrons in counterpropagating Gaussian wave packets

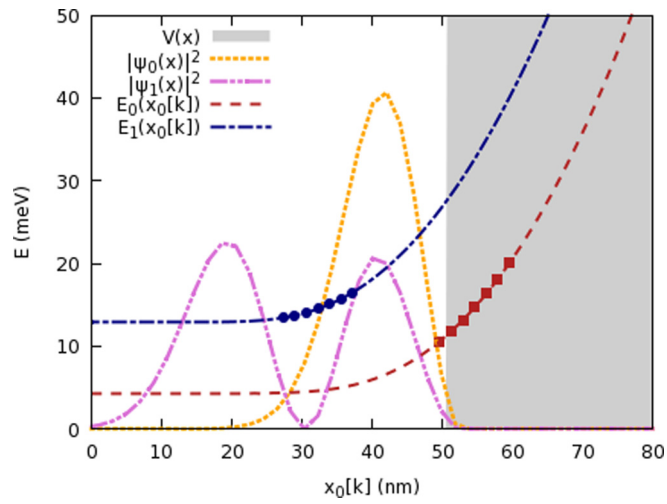

FIG. 2. Band structure of the active region induced by the sharp potential barrier (gray shaded area) for the first three edge channels at $B = 5$ T. The dots define the centers $x_0(k)$ of the edge states contained in the Gaussian wave packets with $n = 0$ and $n = 1$. The transverse profiles of the probability density for a wave packet injected with a central energy $E^0 = 15$ meV and $\sigma = 40$ nm in $n = 0$ and $n = 1$ are also displayed (dashed yellow and purple lines).

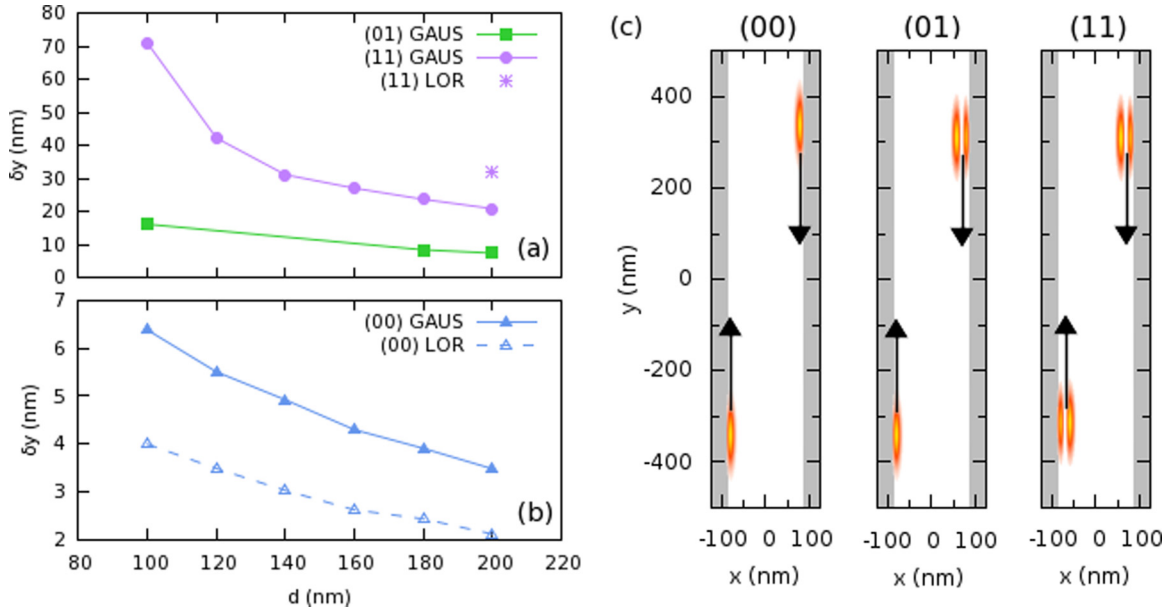

FIG. 3. (a) Spatial shift δy for two indistinguishable electrons in the two excited configurations (01) and (11), with $\sigma = 40$ nm and in the presence of the long-range unscreened Coulomb interaction of Eq. (15) with $d_z = 1$ nm. The label *GAUS* refers to a Gaussian single-electron wave function, while *LOR* to a Lorentzian wave packet. (b) Spatial shift δy for two indistinguishable electrons in the ground configuration (00) with the same parameters as above. (c) Map of the active region of the device with the external potential (gray) and initial density probability distributions of two single-electron wave packets (red) in the three configurations under study: (00) both electrons in the ground channel 0, (01) one electron in channel 0 and one electron in the excited channel 1, (11) both electrons in channel 1. Black arrows define the direction of propagation of the wave packets.

of edge state, by comparing three different configurations labeled as (n_1, n_2) with $n_1 = 0, 1$ and $n_2 = 0, 1$, and simulate their Coulomb-driven scattering by assuming an unscreened long-range soft Coulomb interaction:

$$V_{12} = \frac{e^2}{4\pi\epsilon_r\sqrt{(x_1 - x_2)^2 + (y_1 - y_2)^2 + d_z^2}}, \qquad (15)$$

where ϵ_r is the medium permittivity of GaAs and $d_z = 1$ nm avoids the divergence at $\mathbf{r}_1 = \mathbf{r}_2$ with a negligible effect on the numerical results since the wave functions of the two quasiparticles in the device of Fig. 1 are always spatially well separated, i.e., the joint probability is essentially zero for any two coordinates less than about 100 nm apart.

A. Exact two-electron scattering in 2D

Due to the exchange symmetry, we expect that at the final time (when V_c is negligible due to the large distance between the two electrons) the probability of one of the two particles integrated over the other one shows the same value in the two outputs, as in the initial condition. The effect of Coulomb interaction is then traced to the difference between the final density probability of the second particle in the interacting case and in the noninteracting case, in the direction of propagation (i.e., the y direction of the device). Indeed, when two electrons approach each other, electron-electron repulsion transforms part of their kinetic energy into interparticle potential energy, so that the velocity along their path is reduced. As the relative distance returns then to the original value, the potential energy is transformed back into kinetic energy and the initial velocity is restored. This turns into a delay in the propagation of the two electrons compared to the noninteracting case that corresponds to a phase factor in front of the $|11\rangle$ component of the two-qubit wave function in the global T transformation.

The difference between the maximum of this distribution in the interacting and noninteracting scenario, namely δy, depends on the geometry of the active region. The latter can be strongly affected by the distance between the two lateral edges, the wave-packet size, and the smoothness of the confining barriers. With regards to the last parameter, a proper design of $V(x)$ with sharp lateral barriers is necessary to induce a quasiparabolic dispersion of the second or first Landau level, rather than a linear one, to ensure a measurable δy. Indeed, in the presence of linear dispersion, the change in the kinetic energy of the two wave packets does not change the velocity, so that the displacement δy is zero.

Figures 3(a) and 3(b) compare the values of δy in the three configurations, namely (00), (01), and (11), that are displayed in Fig. 3(c) for a range of distances between the edges, ranging from $d = 100$ to $d = 200$ nm. Note that, as described above, no tunneling is present in this operating regime. The effect of Coulomb repulsion generally decreases with the distance between the two borders of the device d and determines a larger longitudinal shift δy for the configuration with two electrons in the excited channel $n = 1$. This trend agrees with the lower group velocity in the excited edge channel, together with a larger Coulomb interaction due to the transverse spatial distribution of the wave packet for $n = 1$ in Fig. 2. The discrepancy between the values of δy in the three

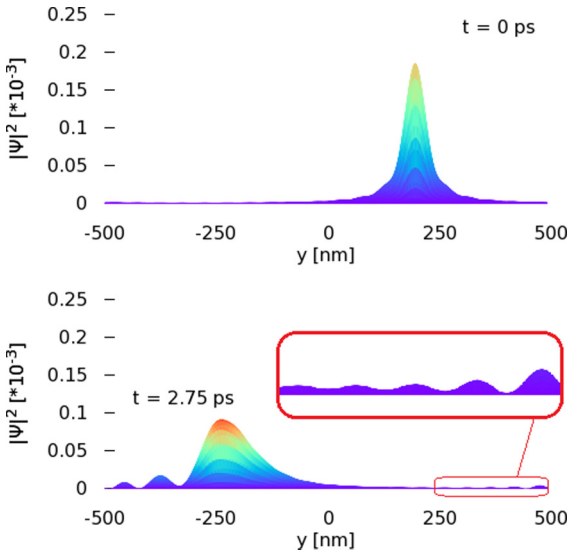

FIG. 4. Single-electron density probability for a Lorentzian wave packet with $\Gamma = 50$ nm and $n = 0$ at (a) initial and (b) final time.

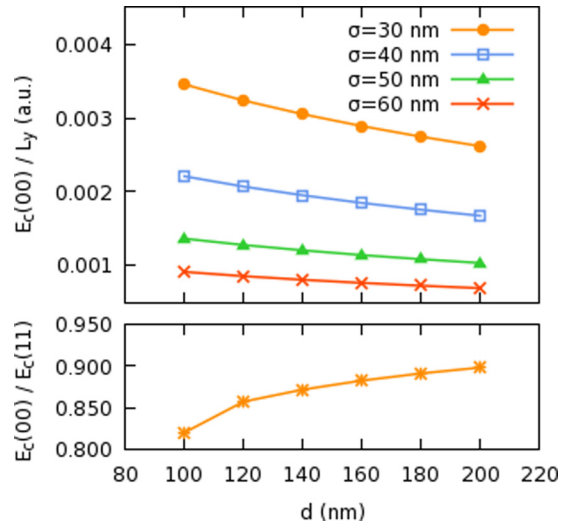

FIG. 5. (Top) Integrated Coulomb energy per length size $\mathcal{E}_c$ in Eq. (17) exchanged during the scattering of two indistinguishable electrons in the (00) configuration as a function of the distance between the edges of the confining potential d for different wave packet sizes σ. (Bottom) Ratio between the integrated Coulomb energy per length size $\mathcal{E}_c$ in the (00) configuration and in the (11) configuration.

cases increases significantly when the distance between the two edges is reduced.

We also remark that the functioning of this solid-state implementation of the conditional phase shifter does not depend qualitatively on the shape of the wave packet. To prove this, we simulate the interaction of two Lorentzian single-electron wave packets in our device, by adopting the numerical model validated for levitons [36,40] in Ref. [41]. In this scenario, the weight function $F(k)$ has an exponential distribution on the Fourier space, so that the wave function is Lorentzian in the real space. Note that the present single-electron excitation operates in the same regime of the Gaussian wave packets. Figure 4(a) displays the initial distribution of the density probability in the longitudinal direction of the real space, while panel (b) shows the same density probability after its evolution in time. Differently from the Gaussian excitation, the Lorentzian pulse does not maintain its shape during the evolution, and oscillations are present in the tail of the density probability. Figure 3 also displays the values of the spatial shift generated by a two-electron scattering in the active region for a Lorentzian wave packet. By simulating the long-range Coulomb-driven interaction for two wave packets in the (00) configuration [Fig. 3(b)], we observe that the trend of the spatial shift does not differ qualitatively from the one computed with the Gaussian modeling of the electron state. Figure 3(a) further shows the value of dy computed by studying the interaction of two Lorentzian states initialized in the excited channel ($n = 1$). In the present case, the computed value for the phase shift is larger than the one predicted in the Gaussian case; this follows from the lower group velocity of the Lorentzian excitation, whose dynamics is more strongly affected by the nonlinearity of the band structure due to the large number of edge states in the tails of the weight distribution. However, also in the Leviton-like modeling of single-electron wave packets, the values of the spatial shifts in the ground and in the excited channel differ by tens of nanometers.

B. Estimate of the interaction energy

To analyze the interplay between the effects related to the different band structures of the Landau levels and the real-space distribution of the charge encoded in the Gaussian wave packets, we estimate the total amount of energy exchanged during the two-electron scattering in the active region. We initially map the Coulomb potential $V_{12}(x_1, y_1, x_2, y_2)$ by fixing the x_1 and x_2 coordinates to the maxima of the single-electron wave packets, namely $x_1 = x_1^M$ in the channel on the right and $x_2 = x_2^M$ in the channel on the left [see Fig. 3(c)]. The Coulomb potential energy $V(x_1^M, y_1, x_2^M, y_2)$ is then averaged over the discrete set of y coordinates that define the path of each edge channel, i.e., $y_1 = -y_2 = Y$ with $Y \in [-L_y, L_y]$, where L_y is the positive coordinate of the boundary in the y direction.

To provide a better estimate of the energy exchanged, we also account for the 2D spatial distribution of the single charge. Therefore, we average the Coulomb potential $V(x_1^*, Y; x_2^*, -Y)$, on a 2D Gaussian distribution $F(x, x^*, y, y^*)$, that is centered in $x^* = x^M$ and $y^* = Y$, i.e.,

$$F(x, x^M, y, Y) = a_x e^{-(x-x^M)^2/2\sigma_x^2} a_y e^{-(y-Y)^2/2\sigma_y^2}, \qquad (16)$$

where σ_x and σ_y are the real-space broadening in the transverse and longitudinal direction, respectively, and a_x and a_y are normalization constants. The integrated Coulomb energy exchanged during the scattering per length size then reads:

$$\mathcal{E}_c = \frac{1}{L_y} \int dY d\mathbf{r}_1 d\mathbf{r}_2 F\left(x_1, x_1^M, y_1, Y\right) \times V\left(x_1^M, Y, x_2^M, -Y\right) F\left(x_2, x_2^M, y_2, -Y\right). \qquad (17)$$

$\mathcal{E}_c$ is displayed in the top panel of Fig. 5 as a function of the distance d for different values of σ. Here, we approximate the spatial distribution of a single-electron wave packet

with $n = 0$ by means of the above Gaussian distribution $F(x, x^M, y, Y)$ with $\sigma_x = 5$ nm and $\sigma_y = \sigma$.

The integrated Coulomb energy $\mathcal{E}_c$ shows that for smaller wave packets the repulsion is larger, as a result of the increase in charge localization. This difference decreases with the distance d, in agreement with the fact that Coulomb repulsion becomes less effective when the electrons are further separated. Note, however, that this simple model does not take into account the real shape of the edge states and their corresponding band structure; indeed, when the distance between the two edges is reduced, the minimum of the Landau level is raised, so that for a given distance of the center $x_0(k)$ to the turning point of the barrier, x_L or x_R, the energy broadening of the wave packets shifts to lower values, thus decreasing the group velocity of the wave packet. This is expected to affect more strongly smaller wave packets in the real space, and therefore at shorter distances δy eventually increases with σ.

Finally, the bottom panel of Fig. 5 displays the ratio between the integrated energy exchanged during the scattering in the (00) configuration and in the (11) configuration, which is—in our operating regime—between 80% and 90%. The large discrepancy between the values of δy in the two configurations does not find an explanation in the amount of Coulomb energy exchanged alone: The different bending of the Landau levels—and therefore the smaller group velocity of the electron in the excited channel—is the origin of this effect.

C. Screening and bunching probability

Besides exposing the spatial shift generated by Coulomb interaction, the exact computation of the four-degrees-of-freedom wave function allows us to measure dynamically the two-electron bunching probability. The real-space domain is partitioned in a *TOP* ($y > 0$) and a *BOTTOM* ($y < 0$) region, which correspond to the outputs of the single-electron wave packets ψ_α and ψ_β, respectively. As in the electron HOM experiment in Ref. [22], we compute the bunching probability as

$$P_b = \int_{S_{\rm TT}} dr_1 dr_2 |\Psi(r_1, r_2)|^2 + \int_{S_{\rm BB}} dr_1 dr_2 |\Psi(r_1, r_2)|^2, \tag{18}$$

where $S_{\rm TT}$ and $S_{\rm BB}$ are 4D domains in the configuration space with $y_1, y_2 > 0$ and $y_1, y_2 < 0$, respectively. We estimate $P_b(t)$ in the two different cases of distinguishable and indistinguishable particles, for two small values of the distance d, namely $d = 30$ and $d = 40$ nm, and in the (00) configuration. Note that, differently from the operating regime of the numerical simulations above (with $d > 100$ nm), the two single-electron wave functions in counterpropagating channels partially overlap in the transverse direction at initial time, so that tunneling between them could occur during the scattering.

The numerical results are displayed in Fig. 6. In this specific case, we reduce the value of the regularization factor d_z by two orders of magnitude in order to allow the two quasiparticles to get close to each other. Still, a finite value of d_z avoids the Coulomb divergence, occurring with the (unphysical) simultaneous localization of the two quasiparticles at a single grid point. We verified that smaller values of the regularization factor do not lead to substantial differences in our results. For the simulated values of the channel distance d and distinguishable particles, we measure a nonzero bunching probability that generally decreases by reducing the distance, and it almost vanishes for $d > 40$ nm. We further observe that, as in the HOM geometry, Coulomb interaction does not fully reflect the two electron, differently from the expected result in an effective 1D geometry. In the latter scenario, indeed, the two electrons are forced to propagate on the same rail, so that at $y_1 = y_2$ they experience diverging value of the Coulomb interaction. Moreover, with contrast to the case of Ref. [22], the bunching probability is fully quenched by the presence of exchange interaction, regardless of the distance between the two rails. Differently from the wave packets generated after the interaction with a quantum point contact, the reflected and transmitted states induced by Coulomb repulsion fully overlap in the Fourier space.

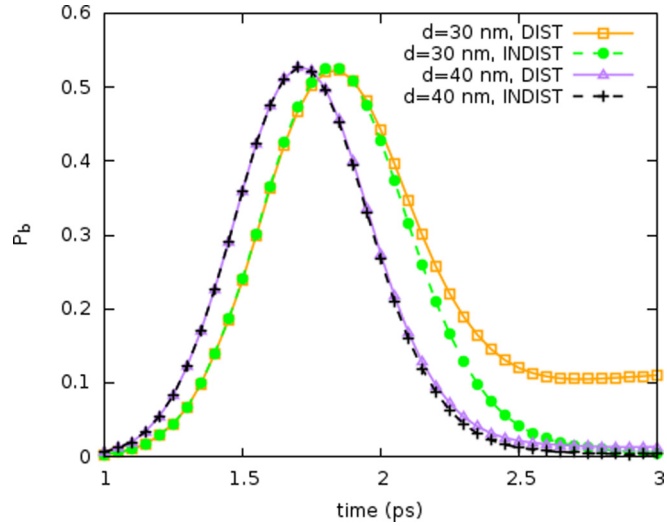

FIG. 6. Bunching probability Pb(t) during the Coulomb-driven scattering for two distinguishable/indistinguishable electrons initialized in Gaussian wave packets with $\sigma = 40$ nm in the (00) configuration for small values of the distance d. Note that tunneling between the two counterpropagating channels is present in this regime.

Finally, we simulate the effect of screening by adding an exponential damping in the Coulomb repulsion:

$$V_{12} = \frac{Ce^2 \exp(-\sqrt{(x_1 - x_2)^2 + (y_1 - y_2)^2}/\sigma_c)}{4\pi\epsilon_r \sqrt{(x_1 - x_2)^2 + (y_1 - y_2)^2 + d_z^2}}, \tag{19}$$

where σ_c is the effective interaction length and C the amplitude of the screening. Top panel of Fig. 7 shows the values of δy in presence of screening for the (00) configuration with $\sigma = 40$ nm and a distance between the edges of the confining barrier that goes from $d = 100$ nm to $d = 200$ nm. In our operating regime, we simulate a damping length σ_c of the order of the width of the active region ($L_x = 250$ nm) and observe that the values of δy are reduced by a factor of at least 1/2. The bottom panel of Fig. 7 compares the spatial shift δy in the three configurations for the largest separation between the edges of the device, $d = 200$ nm, that ensures the absence of interchannel tunneling. We observe that, for a screening length σ_c larger than the distance between the two

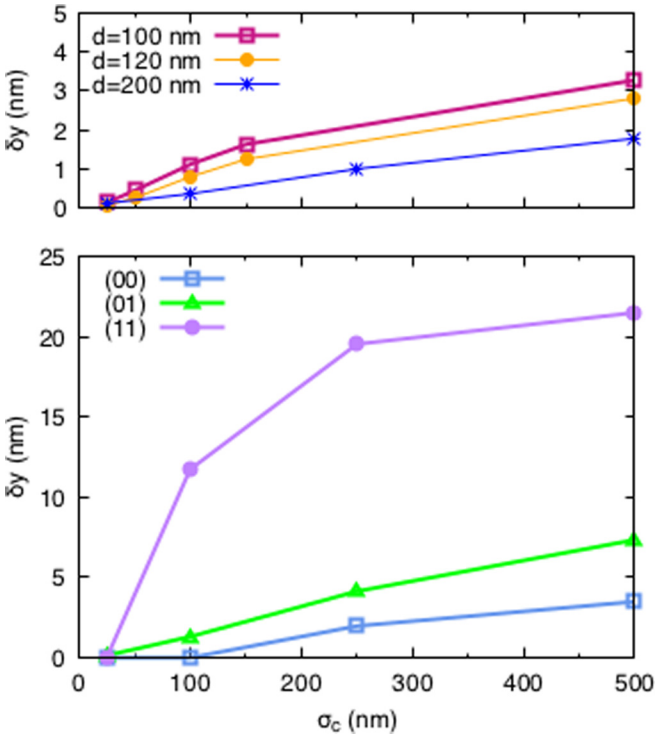

FIG. 7. (Top) Spatial shift δy in the presence of screening for two indistinguishable electrons initialized in wave packets with $\sigma = 40$ nm in the (00) configuration. The value at $\sigma_c = 500$ nm corresponds to δy in presence of unscreened long-range interaction. (Bottom) Comparison between the spatial shifts δy for two indistinguishable electrons with $\sigma = 40$ nm in the three different configurations and $d = 200$ nm with screening.

edges of the device (from 500 nm to 200 nm), δy decreases by about 1 nm regardless of the edge channel where electrons propagate. This decrement does not affect significantly the large value of δy in the (11) case, while the small spatial shift in the two weakly-interacting configurations, (00) and (01), becomes comparable to the resolution of our simulation grid. When the screening parameter σ_c further decreases below the value of d (from 200 nm to 100 nm), the value of δy in the (00) case vanishes, while the one in the (11) configuration is still large and measurable. Moreover, the electron density probability in channel 0 is localized less deeply in the bulk with respect to channel 1 (yellow and purple dashed lines for $0 < x < 50$ nm in Fig. 2); thus, for such values of d, the screened Coulomb repulsion between two (00) charges is suppressed faster by the exponential damping in Eq. (15).

The above results predict that by properly tuning the geometrical parameters of the active region with modulation gates, or by varying the effective length for the screening, e.g., by modifying the electron density of the 2DEG, it is possible to quench the effect of Coulomb repulsion for all configurations except the (11) one, so that electron-electron repulsion acts as a selective entangler also for this simple geometry. The components of the latter device have dimensions that are feasible with current nanotechnology.

In the next section we further simulate the Coulomb-driven scattering between two indistinguishable electrons with a more realistic geometry of the active region that corresponds to the inner part of the loop area in the multichannel Mach-Zehnder interferometer of Ref. [15]; we then predict the phase shift γ that rotates the (11) component of the two-electron wave function in the full-scale conditional phase shifter of Fig. 1(a).

D. The phase shift γ in the T transformation

We now address a more realistic profile of the confining potential and predict the phase γ in the T matrix of Eq. (1) for the full-scale device of Fig. 1(a). First, we model the confining barrier with a smoothed profile in the x direction:

$$V_{\rm ext}(x) = V_b\left(\frac{1}{1+e^{\frac{x-x_b}{\lambda}}} + \frac{1}{1+e^{\frac{-x+x_b}{\lambda}}}\right), \qquad (20)$$

where $V_b = 0.31$ eV, $\lambda = 3$ nm, and $x_b = 55$ nm. Figure 1(b) compares the potential profile in the transverse direction of the device (blue shaded area), to the band structure of the second Landau level (blue solid line) and the density probability of a single electron wave packet with $n = 1$, $\sigma = 40$ nm, and an injection energy of $E^0 = 20.4$ meV (black dashed line). Note that this regime reproduces the geometry and the injection protocol of the multichannel MZI described in Ref. [15], which is the building block of our proposal for a solid-state implementation of the conditional phase shifter.

Consistently to the findings in the simplified model presented above, we expect a stronger Coulomb interaction between the counterpropagating electrons with both Landau levels $n = 1$. The sharper bending of the first Landau level determines a smaller magnetic mass m_B^* with respect to a wave packet with the same energy distribution but higher cyclotron index n. The smaller group velocity for $n = 1$ induces a larger shift in the real-space δy. Moreover, at a given value of the injection energy $E^0(k)$, the center $x_0^n(k)$ of an edge state with $n = 0$ is closer to the profile of the confining barrier with respect to the corresponding edge state with $n = 1$. The transverse probability distribution of two wave packets in the second Landau level is then larger in the bulk with respect to the case of two wave packets initialized in the ground state, thus enhancing the effect of Coulomb interaction.

The relation between the spatial shift δy and the γ factor in the **T** matrix cannot be trivially determined by the wave vector k alone, due to its gauge dependence. We resort to the difference in the optical paths $L_{\rm eff}$, that is necessary to produce a 2π rotation in each single-electron MZI at the edge of the device.

By means of a single-particle solver, we simulate the dynamics of single-electron interference in one of the two Mach-Zehnder interferometers reported in Fig. 1(a). Here, we artificially introduce a relative shift in the y direction (ΔY) between the two components of the wave function in the loop area. This spatial shift corresponds to a relative phase factor in the single-electron wave function between the transmitted wave packet in $n = 0$ and the transmitted one in $n = 1$ after the scattering with the potential dip labeled as BS1 in Fig. 1(a). In a full-scale two-qubit device, the introduction of an artificial shift ΔY mimics the effect of Coulomb repulsion on the electron in the excited edge channel, when the counterpropagating electron is in the active region [yellow box in Fig. 1(a)]. In the equivalent single-electron simulation,

ΔY rotates the final state at the output of the MZI. The spatial periodicity $L_{\rm eff}$ of the interference pattern in the transmission amplitude for the 0 channel, $T(\Delta y)$, is then related to γ: If $L_{\rm eff}$ corresponds to a 2π rotation in the output state of a single-electron Mach-Zehnder experiment, the same rotation, $\gamma = 2\pi$, is obtained by introducing a selective Coulomb repulsion that shifts the final position of the two wave packets in $n = 1$ by a factor $\delta y = L_{\rm eff}$. Within the present regime, we measure an effective length $L_{\rm eff} = 20$ nm. The dynamical simulation of the Coulomb-driven scattering of two indistinguishable electrons in the second edge channel provides the shift δy for the present realistic geometry, which is measured to be $\delta y = 11$ nm.

We finally relate the shift δy to the corresponding γ in the T transformation in Eq. (1) by using $L_{\rm eff}$ as a reference and resorting to the following equation:

$$\gamma = 2\pi \frac{\delta y}{L_{\rm eff}}, \tag{21}$$

which provides $\gamma = \pi$ in the full-scale conditional phase shifter. This proves the feasibility of a selective phase shifter with a factor π in our geometry, where the smoothed barriers are characterized by a relative distance $W = 110$ nm at $B = 5$ T. Moreover, in our model the value of γ and the spatial shift δy are related only by the screening-independent parameter $L_{\rm eff}$, computed from the single-electron interference pattern in an isolated MZI. Then, a proper increase of the distance between the outer edges of the two mesas at the nanometer scale can be eventually combined with a controlled manipulation of the screening parameter σ_c to induce a rotation that ranges from $\pi/2$ to 2π, thus making this device a viable approach for conditional phase shifting driven by Coulomb interaction.

IV. CONCLUSIONS

We have shown that Coulomb interaction between two charge carriers moving in two counterpropagating edge channels can induce a consistent and controllable phase shift in one of the four configurations of possible Landau levels occupancy. By encoding a qubit state into the Landau level index degree of freedom of one of the carriers, with only two Landau levels being energetically accessible, the above phase only applies to the (11) state, thus creating a two-qubit conditional phase shifter T. The quantum gate T can be adopted, in turn, as the two-qubit entangling transformation of a universal set of quantum gates.

Our simulations address the numerically exact propagation of the two-particle wave function in a full-scale geometry of a device operating at bulk filling factor two. Thus, all the real-space effects of the electron-electron mutual interaction are accounted for, including the generation of quantum correlations between the longitudinal degrees of freedom (i.e., the particle positions along the edge channels) and the effect of the finite localization of the carriers. Indeed, we found that the higher the spatial localization, the stronger the effect of Coulomb interaction. Also, a Lorentzian shape of the charge carrier wave function gives rise to the same entanglement effect as a Gaussian wave packet, although the low-energy tail reduces in average the phase of the T transformation.

Most important, we demonstrated that the conditional phase generated by the multiedge state device can be as large as π and its value can be controlled by the static confinement potential. We emphasize that our multichannel proposal of two-electron interferometry and controlled entanglement generation, although general in its basic ideas, is based on the only scalable platform available for an interferometer of the Mach-Zehnder type in the IQH regime. Single-channel [7,20] or Corbino setups [11] adopted in the past are indeed characterized by an Ohmic contact inside the loop area that is not required in our scenario [13]. Within our model, we observe the evolution and interference of single-electron wave packets and reproduce the dynamics of quasiparticles generated from single-electron sources, nowadays feasible in the IQH regime [34,36,37]. Moreover, their propagation in cyclotron-resolved channels instead of spin-resolved ones [14,29], together with the presence of a tunable potential mesa and small beam splitters, is proved [15] to shorten the distance of copropagation and to reduce decoherence phenomena arising from interchannel interactions, as charge fractionalization [42]. Additionally, recent theoretical studies [43] and experimental works [44,45] observe that a proper tuning of the energy distribution for the emitted carrier and the magnetic regime allows controlling the relaxation processes induced by inelastic scattering with acoustic and optical phonons.

ACKNOWLEDGMENTS

This work has been co-funded by the European Union Horizon 2020 Research and Innovation Programme through the FET Open project IQubits under Grant Agreement No. 829005. We also acknowledge CINECA for HPC computing resources and technical support under the ISCRA C initiatives QUPIDO (HP10CPRABZ) and CHINHEX (HP10CEMC7B). PB and AB are members of gnfm-INdAM. We thank Prof. Xavier Oriols for useful discussions.

[1] C. Grenier, R. Herv, G. Fve, and P. Degiovanni, Mod. Phys. Lett. B **25**, 1053 (2011).
[2] B. Roussel, C. Cabart, G. Fve, E. Thibierge, and P. Degiovanni, Phys. Status Solidi (b) **254**, 1600621 (2017).
[3] D. C. Glattli and P. S. Roulleau, Phys. Status Solidi (b) **254**, 1600650 (2017).
[4] E. Locane, P. Brouwer, and V. Kashcheyevs, New J. Phys. **21**, 093042 (2019).
[5] R. H. Rodriguez, Relaxation of quasiparticles injected above the Fermi sea of a quantum Hall edge channel, Ph.D. thesis, Université Paris-Saclay, 2019 (unpublished).
[6] Y. Ji, Y. Chung, D. Sprinzak, M. Heiblum, D. Mahalu, and H. Shtrikman, Nature (London) **422**, 415 (2003).
[7] I. Neder, M. Heiblum, Y. Levinson, D. Mahalu, and V. Umansky, Phys. Rev. Lett. **96**, 016804 (2006).
[8] K. Kang, Phys. Rev. B **75**, 125326 (2007).

[9] H. V. Lepage, A. A. Lasek, D. R. M. Arvidsson-Shukur, and C. H. W. Barnes, Phys. Rev. A **101**, 022329 (2020).
[10] P. Roulleau, F. Portier, P. Roche, A. Cavanna, G. Faini, U. Gennser, and D. Mailly, Phys. Rev. Lett. **100**, 126802 (2008).
[11] E. V. Deviatov, A. Ganczarczyk, A. Lorke, G. Biasiol, and L. Sorba, Phys. Rev. B **84**, 235313 (2011).
[12] A. Beggi, P. Bordone, F. Buscemi, and A. Bertoni, J. Phys.: Condens. Matter **27**, 475301 (2015).
[13] V. Giovannetti, F. Taddei, D. Frustaglia, and R. Fazio, Phys. Rev. B **77**, 155320 (2008).
[14] B. Karmakar, D. Venturelli, L. Chirolli, V. Giovannetti, R. Fazio, S. Roddaro, L. N. Pfeiffer, K. W. West, F. Taddei, and V. Pellegrini, Phys. Rev. B **92**, 195303 (2015).
[15] L. Bellentani, A. Beggi, P. Bordone, and A. Bertoni, Phys. Rev. B **97**, 205419 (2018).
[16] W. D. Oliver, J. Kim, R. C. Liu, and Y. Yamamoto, Science **284**, 299 (1999).
[17] M. Büttiker, P. Samuelsson, and E. Sukhorukov, Physica E: Low-dimensional Syst. Nanostruct. **20**, 33 (2003), proceedings of the International Symposium "Quantum Hall Effect: Past, Present and Future".
[18] V. S.-W. Chung, P. Samuelsson, and M. Büttiker, Phys. Rev. B **72**, 125320 (2005).
[19] P. Samuelsson, E. V. Sukhorukov, and M. Büttiker, Phys. Rev. Lett. **92**, 026805 (2004).
[20] I. Neder, N. Ofek, Y. Chung, M. Heiblum, D. Mahalu, and V. Umansky, Nature (London) **448**, 333 (2007).
[21] D. Glattli and P. Roulleau, Physica E: Low-dimensional Syst. Nanostruct. **76**, 216 (2016).
[22] L. Bellentani, P. Bordone, X. Oriols, and A. Bertoni, Phys. Rev. B **99**, 245415 (2019).
[23] D. Ferraro, F. Ronetti, L. Vannucci, M. Acciai, J. Rech, T. Jockheere, T. Martin, and M. Sassetti, Eur. Phys. J.: Spec. Top. **227**, 1345 (2018).
[24] A. Marguerite, C. Cabart, C. Wahl, B. Roussel, V. Freulon, D. Ferraro, C. Grenier, J.-M. Berroir, B. Plaçais, T. Jonckheere, J. Rech, T. Martin, P. Degiovanni, A. Cavanna, Y. Jin, and G. Fève, Phys. Rev. B **94**, 115311 (2016).
[25] D. Marian, E. Colomés, and X. Oriols, J. Phys.: Condens. Matter **27**, 245302 (2015).
[26] C. Wahl, J. Rech, T. Jonckheere, and T. Martin, Phys. Rev. Lett. **112**, 046802 (2014).
[27] A. Bertoni, P. Bordone, R. Brunetti, C. Jacoboni, and S. Reggiani, Phys. Rev. Lett. **84**, 5912 (2000).
[28] P. Bordone, L. Bellentani, and A. Bertoni, Semicond. Sci. Technol. **34**, 103001 (2019).
[29] L. Chirolli, F. Taddei, R. Fazio, and V. Giovannetti, Phys. Rev. Lett. **111**, 036801 (2013).
[30] See Supplemental Material at http://link.aps.org/supplemental/10.1103/PhysRevB.102.035417 for an animation of the two-electron dynamics in the proposed conditional phase shifter formed by the gray potential landscape.
[31] T. Kramer, C. Kreisbeck, and V. Krueckl, Phys. Scr. **82**, 038101 (2010).
[32] M. Büttiker, H. Thomas, and A. Prêtre, Phys. Lett. A **180**, 364 (1993).
[33] A. Mahé, F. D. Parmentier, E. Bocquillon, J.-M. Berroir, D. C. Glattli, T. Kontos, B. Plaçais, G. Fève, A. Cavanna, and Y. Jin, Phys. Rev. B **82**, 201309 (2010).
[34] E. Bocquillon, V. Freulon, J.-M. Berroir, P. Degiovanni, B. Plaçais, A. Cavanna, Y. Jin, and G. Fève, Science **339**, 1054 (2013).
[35] M. D. Blumenthal, B. Kaestner, L. Li, S. Giblin, T. J. B. M. Janssen, M. Pepper, D. Anderson, G. Jones, and D. A. Ritchie, Nat. Phys. **3**, 343 (2007).
[36] J. Dubois, T. Jullien, F. Portier, P. Roche, A. Cavanna, Y. Jin, W. Wegscheider, P. Roulleau, and D. C. Glattli, Nature (London) **502**, 659 (2013).
[37] M. Kataoka, J. D. Fletcher, and N. Johnson, Phys. Status Solidi (b) **254**, 1600547 (2017).
[38] C. Bauerle, D. C. Glattli, T. Meunier, F. Portier, P. Roche, P. Roulleau, S. Takada, and X. Waintal, Rep. Prog. Phys. **81**, 056503 (2018).
[39] S. Ryu, M. Kataoka, and H.-S. Sim, Phys. Rev. Lett. **117**, 146802 (2016).
[40] F. Ronetti, M. Carrega, and M. Sassetti, Phys. Rev. Research **2**, 013203 (2020).
[41] J. Keeling, I. Klich, and L. S. Levitov, Phys. Rev. Lett. **97**, 116403 (2006).
[42] C. Cabart, B. Roussel, G. Fève, and P. Degiovanni, Phys. Rev. B **98**, 155302 (2018).
[43] C. Emary, L. A. Clark, M. Kataoka, and N. Johnson, Phys. Rev. B **99**, 045306 (2019).
[44] Y. Yin, J. Phys.: Condens. Matter **30**, 285301 (2018).
[45] Y. Yin, J. Phys.: Condens. Matter **31**, 245301 (2019).